Ni/Fe based bimetallic coordination complexes with rich active sites for efficient oxygen evolution reaction

Wenzhong Huang[a,1], Chuanxi Chen[a,1], Zhaohong Ling[a,1], Jiantao Li[a,*], Longbing Qu[c], Jiexin Zhu[a], Wei Yang[a], Manman Wang[d], Kwadwo Asare Owusu[a], Ling Qin[a], Liang Zhou[a,*], Liqiang Mai[a,b,*]

[a] State Key Laboratory of Advanced Technology for Materials Synthesis and Processing, School of Materials Science and Engineering, Wuhan University of Technology, Wuhan 430070, Hubei, China
[b] Foshan Xianhu Laboratory of the Advanced Energy Science and Technology Guangdong Laboratory, Xianhu Hydrogen Valley, Foshan 528200, China
[c] Department of Mechanical Engineering, University of Melbourne, Parkville, VIC 3010, Australia
[d] Advanced Technology Institute, University of Surrey, Guildford, Surrey GU2 7XH, United Kingdom

HIGHLIGHTS

- The low-crystalline MCCs (Ni/Fe-MI/OH) with hybrid ligands are constructed.
- The successful coordination of metal ions and hybrid ligands has been verified.
- This structure possess abundant active sites and enhanced mass transport for OER.
- A low overpotential of 229 mV at 10 mA cm^{-2} is obtained.

GRAPHICAL ABSTRACT
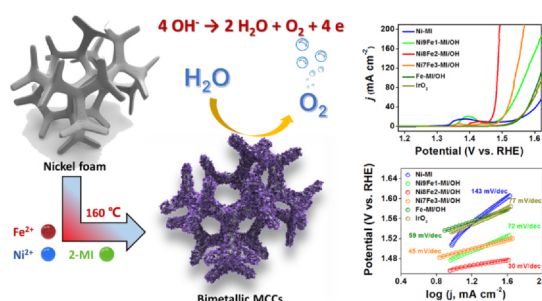
ARTICLE INFO

ABSTRACT

Efficient electrocatalysts are vital for accelerating the sluggish oxygen evolution reaction (OER). Metal coordination complexes (MCCs) consisting of central metals and surrounding ligands generally possess abundant active sites owing to the rich boundaries between short-range crystalline components, making them promising candidates for tailored electrocatalysts. Herein, Ni/Fe based bimetallic MCCs with hybrid ligands are successfully constructed. With rich active sites residing in nanocrystal boundaries, bimetallic synergistic effect, and quick mass transfer derived from the nanosheet-like structure, excellent OER performance in terms of overpotential (229 mV at 10 mA cm^{-2}) and Tafel slope (30 mV dce^{-1}) is achieved. This unique architecture can shed light on the coordination design of highly efficient OER electrocatalysts.

1. Introduction

Developing renewable energy conversion and storage technologies is an important strategy to alleviate the social energy crisis and build a low-carbon society. Electrochemical water splitting for hydrogen production is one of the promising choices [1–4]. As the key anodic reaction of electrochemical water splitting, oxygen evolution reaction (OER) is of great significance but suffers from sluggish kinetics owing to

the high activation energy of four-electron-transfer OER process. Thus, exploiting highly efficient OER catalysts has been the heart of electrochemical water splitting. Currently, limited by the scarcity and high cost, noble metal-based catalysts (IrO_2, RuO_2, etc.) cannot satisfy the scale-up application yet [5,6]. Therefore, the exploration of highly efficient, stable, and low-cost OER catalysts is still a formidable challenge for decreasing the overall working potential of electrochemical water splitting.

Metal coordination complexes (MCCs), an emerging class of co-ordination materials, are constructed by metal ions and organic/inorganic surrounding ligands [7,8]. Due to the distinct geometrical spatial arrangement (usually without specific crystalline structure) regulated by different coordination blocks, MCCs have received extensive attention in many fields. For instance, Caruso *et al.* reported a series of low-crystalline/amorphous MCCs by coordinating various transition metal ions with tannic acid [9–12]. The achieved MCCs are stable in a wide pH range, and can be potentially applied in drug delivery and catalysis. Moreover, Byon *et al.* designed a sequence of cobalt–polypyridyl complexes with different redox potentials through regulating the number of pyrazoles in the ligand [13]. When these MCCs were applied as the catholytes and anolytes of redox flow batteries, the batteries showed relatively high output voltage, and stable cycling performance. In the specific area of electrocatalysis, MCCs with long-range disorder and short-range order can create rich active sites residing in abundant boundaries owing to the unique structure constructed by both different metal ions and hybrid surrounding ligands. Besides, the adjustable ligands and metal species make it easy to modify the adsorption energy of reaction intermediates during the OER, thus benefiting the OER process. Therefore, MCCs with tailored structure exhibit a high potential to be used as OER catalysts. Recently, Yu *et al.* reported an amorphous Fe/Co coordination complex with abundant bimetallic centers located at its three-dimensional (3D) hierarchical architecture through a ligand competition strategy [14]. When applied as an OER catalyst, this amorphous structure demonstrated an excellent activity with a low overpotential of 249 mV at 10.0 mA cm^{-2} and a low Tafel slope of 39.5 mV dec^{-1}. On the other hand, the synergistic effect between different metal active sites would strengthen the electrocatalytic performance for OER [15–18]. Ni/Fe based catalysts, such as NiFe oxides [16], NiFe-based metal organic frameworks (MOFs) [17], and NiFe-based layered double hydroxides (LDHs) [18], have gained much attention in OER due to their low cost and high activity. Unfortunately, until now, only a handful of studies on NiFe-based MCCs with hybrid ligands for electrochemical water splitting have been reported. In this regard, developing facile tactics to synthesize NiFe-MCCs with rich active sites, boosted mass transport, as well as prolonged durability is highly promising.

Herein, a facile strategy is developed to prepare Ni/Fe based bimetallic coordination complexes with the hybrid ligands of 2-methylimidazole (2-MI) and hydroxyl (donated as NiFe-MI/OH). Through spectroscopic measurements, the hybrid coordination mechanism is revealed: the presence of Fe ions can effectively promote the co-ordination of metal ions and ligands, and this special coordination situation could lead to the loss of long-range order which benefits for the generation of abundant boundaries and active sites for OER. In addition, the unique nanosheet structure can shorten the electron/ion transport pathways. When applied as an OER catalyst, the NiFe-MI/OH demonstrates excellent OER performance in terms of overpotential (229 mV at 10 mA cm^{-2}) and Tafel slope (30 mV dec^{-1}). Moreover, the exploration of this kind of coordination complexes could open a new avenue for designing next-generation OER catalysts with high performance.

2. Experiment section

2.1. Synthesis of NiFe-MI/OH

Nickel foam (NF) was cleaned and activated with ethanol, acetone, dilute hydrochloric acid, and deionized water in sequence. Solution A was prepared via dissolving $Ni(NO_3)_2 \cdot 6H_2O$ (*x* mmol) and $FeSO_4 \cdot 7H_2O$ (1-*x* mmol, *x* = 1, 0.9, 0.8, 0.7, 0) in 20 mL methanol. 4 mmol 2-MI was dissolved in 20 mL methanol to obtain solution B. Solution B was then added dropwise to solution A under continuous stirring. After stirring at 25 degrees for 1 h, the "A + B" solution would be kept at 160 degrees for another 12 h with a slice of as-prepared NF (3 × 5 cm^2) immerged. The end product grown on NF was washed with methanol for three times. Then, the powders were also collected from the bottom and washed with methanol. Lastly, the NiFe-MI/OH that grown on NF and the powders were obtained after drying.

2.2. Preparation of IrO$_2$ loaded on NF

5 mg of IrO_2 was added in a 1 mL solution containing 750 μL iso-propanol, 200 μL deionized water, and 50 μL of Nafion solution (5% for weight). The mixed IrO_2 ink was sonicated to obtain a uniform dispersion liquid and then loaded on NF. Concretely, the total loading amounts of IrO_2 catalysts were about 2.0 mg cm^{-2}.

2.3. Materials characterization

X-ray diffraction (XRD) patterns were performed by a Bruker D8 Discover X-ray diffractometer with a Cu Kα source (λ = 1.054056 Å). In addition, the lattice fringes were obtained via Bragg's law:

$$2d \times sin\theta = n \times \lambda$$

where d is the spacing between the planes in the atomic lattice, θ is the angle between the incident ray and the scattering planes, n is an integer determined by the order given (1, 2, 3…), λ is the wavelengths of X-rays (1.054056 Å).

Transmission electron microscopy (TEM), High-angle annular dark-field scanning transmission electron microscopy (HAADF-STEM) and selected area electron diffraction (SAED) were collected on a Titan G2 60-300 with image corrector. Energy-dispersive X-ray (EDX) spectra were carried out using an Oxford IE250 system. Scanning electron microscopy (SEM) images were obtained at an acceleration voltage of 15 kV with a JEOL-7100F scanning electron microscope. X-ray photo-electron spectroscopy (XPS) measurements and Inductively Coupled Plasma (ICP) measurements were achieved using an ESCALAB 250Xi instrument and an ICP-Prodigy, respectively. Fourier-transform infrared (FT-IR) spectra were performed on a Nicolet 6700. Raman spectra were recorded using a confocal Raman microscope (DXR, Thermo-Fisher Scientific) with 532 nm excitation from an argon ion laser.

2.4. Electrochemical measurements

Electrochemical measurements of NiFe-MI/OH on NF were characterized on a CHI 760D workstation with a rotating-disk-electrode (RDE) system (PINE research instruments, US). The as-synthesized NiFe-MI/OH on NF was cut into 1 cm^2-pieces and served as the working electrode (WE). The saturated calomel electrode (SCE) and graphite rod were served as the reference electrode (RE) and counter electrode (CE), respectively.

Specially, the WE was prepared as follows: firstly, the uniform ink of other catalysts was prepared following the same method for preparing IrO_2 ink. Then 10 μL obtained catalyst ink was uniformly loaded on the glassy carbon (GC) electrode (5 mm in dimeter). The GCE could be used as the WE after drying in air. The preparation of IrO_2 based WE is the same except IrO_2 was used as the catalyst.

In the three-electrode system, the electrolyte was prepared by

dissolving high-purity KOH in deionized water (18.2 5 MΩ cm^{-1}). For better infiltration of samples, all the samples were activated by 50 cyclic voltammetry (CV) cycles at a scan rate of 50 mV s^{-1} in the potential window of 0.1 ~ 0.8 V *vs.* SCE. Linear sweep voltammetry (LSV) curves for NiFe-MI/OH on NF and NiFe-MI/OH powders were carried out at scan rates of 5 and 20 mV s^{-1}, respectively. Electrochemical impedance spectroscopy (EIS) was performed from 1000 kHz to 0.1 Hz to collect the resistance of uncompensated series. *iR* drop was corrected using the uncompensated series resistance.

To study electrochemically active surface areas (ECSAs), CV measurements were performed in the non-Faradaic region (-0.04–0.06 V *vs.* SCE) at different scan rates (20, 40, 60, 80 and 100 mV s^{-1}), and the derived double-layer capacitance (C_{dl}) was used to further assess the ECSA. The value of C_{dl} equals the slope of the fitting line of $\Delta J = (Ja - Jc)/2$ against scan rates, while *Ja* and *Jc* represent the anodic and cathodic currents at 0.01 V *vs.* SCE, respectively. We selected the $-0.04 - 0.06$ V (*vs.* SCE) region to characterize the C_{dl} of the electrocatalyst because this is a non-Faradaic region without redox reactions occurring, which makes the accurate evaluation of C_{dl} feasible.

The C_{dl} can be further converted into ECSA using the specific capacitance value for a standard with 1 cm^{-2} of real surface area. The specific capacitance of NF can be regarded as the standard (1.33 mF cm^{-2}) in the following calculation. The ECSA of each catalyst can be evaluated as follows:

$$A_{ECSA} = \frac{C_{dl} - catalyst\,(mFcm^{-2})}{C_{dl} - GCelectrode\,(mFcm^{-2})perECSAcm^{-2}}$$

The turnover frequency (TOF) is evaluated by the following equation:

$$TOF = \frac{j \times A}{4 \times F \times n}$$

where *j* is current density at the overpotential of 330 mV, A is the effective surface area of the GC (0.196 cm^2), 4 is the electron transfer number during OER. Besides, F is the Faraday constant (C mol^{-1}), and *n* (mol) is the number of active sites. Specially, Ni and Fe atoms of NiFe-MI/OH are regarded as the active sites and *n* is calculated based on ICP results:

$$n = \frac{\frac{m_{catalyst} \times C_{wt\%-Fe}}{M_{Fe}} + \frac{m_{catalyst} \times C_{wt\%-Ni}}{M_{Ni}}}{A_{electrode}}$$

where m$_{catalyst}$ is the catalyst loading on the disk electrode (0.05 mg), C$_{wt\%}$ is the concentration of metal derived from ICP. Besides, A$_{electrode}$ is the geometrical area of RDE (around 0.196 cm^2).

In addition, all the data of measurements were recorded in alkaline electrolyte (1 M KOH, pH = 13.62). The potentials were converted to *vs.* reversible hydrogen electrode (RHE) via the equation: E(RHE) = E (SCE) + 0.0592pH + 0.24. Besides, the overpotential at 10 mAcm^{-2} (@10 mAcm^{-2}) is obtained via the equation: η@10 mAcm^{-2} = E(@10 mAcm^{-2}, V *vs* RHE) – 1.23.

3. Results and discussion

A facile solvothermal strategy has been developed to synthesize the Ni/Fe bimetallic coordination complexes (Scheme 1). Briefly, a homogeneous precursor solution is firstly prepared by mixing metal sources (Ni^{2+}/Fe^{2+}) and 2-MI in methanol. Then a piece of NF was submerged in the solution for solvothermal reaction. In order to explore the influence of composition, five samples with different Ni/Fe ratios are prepared (Ni/Fe = 1/0, 9/1, 8/2, 7/3, 0/1). The actual metallic molar ratios of the final products are determined by ICP, and the ICP results (Fig. S1) show that the actual metallic molar ratios are consistent with the original feeding ratios. It is believed that, during the solvothermal process, dissociated 2-MI or/and hydroxyl (–OH) derived from methanol will coordinate with metal ions to form the final bimetallic

coordination complexes, which will be proved and further discussed in detail. Based on the Ni/Fe feeding molar ratios and the coordinated ligands, the final products are denoted as Ni-MI, Ni9Fe1-MI/OH, Ni8Fe2-MI/OH, Ni7Fe3-MI/OH, and Fe-MI/OH.

The Ni-MI grown on NF is composed of numerous vertically interconnected nanosheets (Fig. S2). With the increment of Fe/Ni, the size of nanosheets decreases gradually, and the nanosheets finally transform into nanoparticles. The corresponding powder collected at the bottom of autoclave exhibits the same tendency: the morphology evolved from nanosheets for Ni-MI/OH to nanoparticles for Fe-MI/OH. It can be inferred that the Ni/Fe-MI/OH grown on the NF and the precipitate at the bottom are the same coordination complexes due to their similar morphology and growing environment.

XRD was employed to monitor the phase conversion of Ni/Fe-MI/OH. To avoid the strong signals from NF, the powders collected from the bottom of autoclaves were analyzed by XRD. Obviously, the Ni-MI exhibits relatively high crystallinity and the representative diffractions can be indexed to the Ni-ZIF metal–organic framework (Fig. 1a) as previously reported [19]. However, the intensity of diffractions decreases sharply with the introduction of Fe species, and only the peaks with lattice distances of 2.64 and 1.53 Å can be observed for Ni9Fe1-MI/OH, Ni8Fe2-MI/OH, and Ni7Fe3-MI/OH. No peaks are retained in the pattern of Fe-MI, suggesting the formation of low-crystalline and even amorphous structure. The evolution from crystalline to amorphous structure is probably caused by the introduction of iron into the Ni-ZIF framework. Moreover, this introduction would change the arrangement of the original lattice and lead to the long-range disorder [17,20].

To determine the coordination environment, especially the surrounding ligands coordinated with metal ions, FT-IR spectra of the Ni/Fe-MI/OH were recorded. The peaks assigned to the stretch of C-N (1438 cm^{-1}) and C=N (1595 cm^{-1}), as well as the peaks belonging to the stretch (1108 cm^{-1}) and the vibration (1680 cm^{-1}) of unoxidized C=C bond can be observed in the 2-MI spectrum (Fig. 1b) [21]. The peak at around 1310–1370 cm^{-1} can be attributed to the C–C aromatic stretching [22]. Compared with 2-MI, the blue shift in FT-IR of Ni/Fe-MI/OH might be caused by the introduction of Fe and hydroxyl. The above peaks can still be observed in the Ni/Fe-MI/OH spectra although there are some peak shifts and intensity weakening, proving that 2-MI exists in the as-prepared samples as ligands. Moreover, as shown in the Ni/Fe-MI/OH spectra, the pristine aliphatic C–H stretch of 2-MI located at 3130 cm^{-1} shifts to 2920 cm^{-1}, and N–H stretch of 2-MI located at 3180 cm^{-1} disappears, strongly suggesting the interaction between Ni/Fe and 2-MI [23]. The vibration bands ascribed to metal-N are often located at low wavenumbers (1000–400 cm^{-1}), and the bands at around 500 cm^{-1} may be assigned to Ni-N and Fe-N vibrations, further confirming the coordination between Ni/Fe and 2-MI [24]. Besides, control experiment (Fig. S3) was carried out without adding 2-MI, which also demonstrated that 2-MI is of great significance during the formation of MCCs. In addition, broad bands at 3420 cm^{-1} caused by O–H stretch can be found. This reveals that –OH as the ligands would also have coordinated with metal ions[21].

Raman spectra of 2-MI and different samples were collected to study the evolution of structural and surface properties (Fig. S4). The peak at 674 cm^{-1} could be observed in all samples, which can be ascribed to the C-CH$_3$ vibration and could be used to confirm the existence of 2-MI in samples [25]. As for Ni/Fe-MI/OH, the emerging peaks at around 470 and 530 cm^{-1} could be used to confirm the existence of metal-O (H) and metal-O, respectively [26]. Based on the analysis above, it can be concluded that 2-MI together with –OH may act as the hybrid ligands for coordinating with Ni/Fe to form MCCs [27,28].

In Fig. 2, XPS was carried out to gain insights into the surface chemistry. In Fig. S5a the survey spectrum of Ni8Fe2-MI/OH displays characteristic peaks of Ni, Fe, N, C, and O. For Ni XPS spectrum, two peaks assigned to Ni 2p$_{3/2}$ (856.1 eV) and Ni 2p$_{1/2}$ (873.7 eV) are exhibited, and the corresponding satellite peaks are located at 861.8 and 879.7 eV. The peaks of Ni spectrum are characteristic peaks for Ni^{2+}
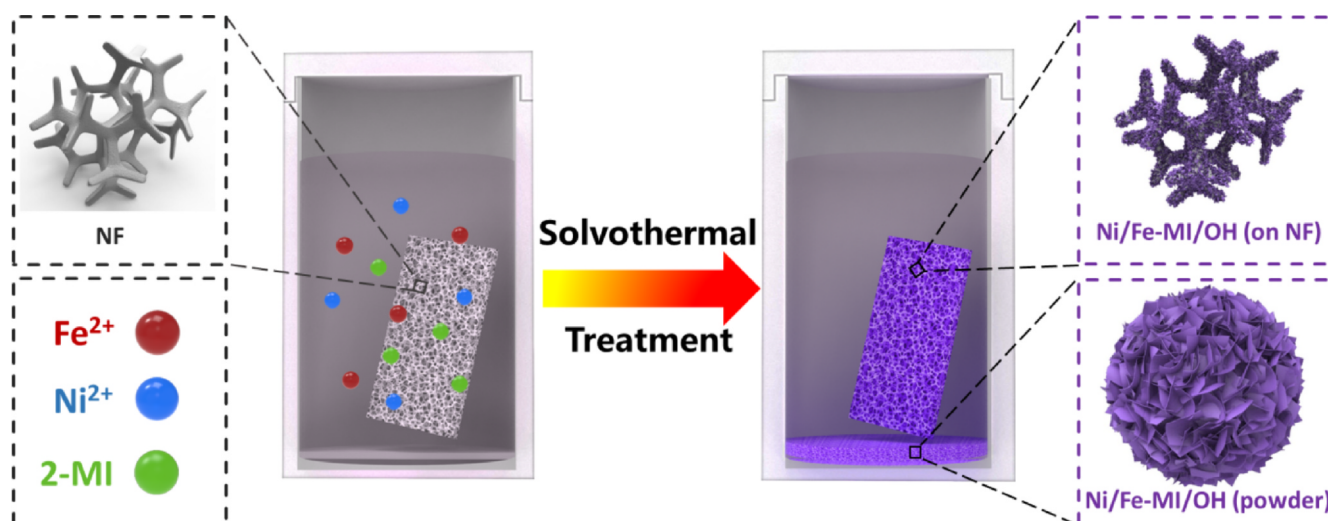
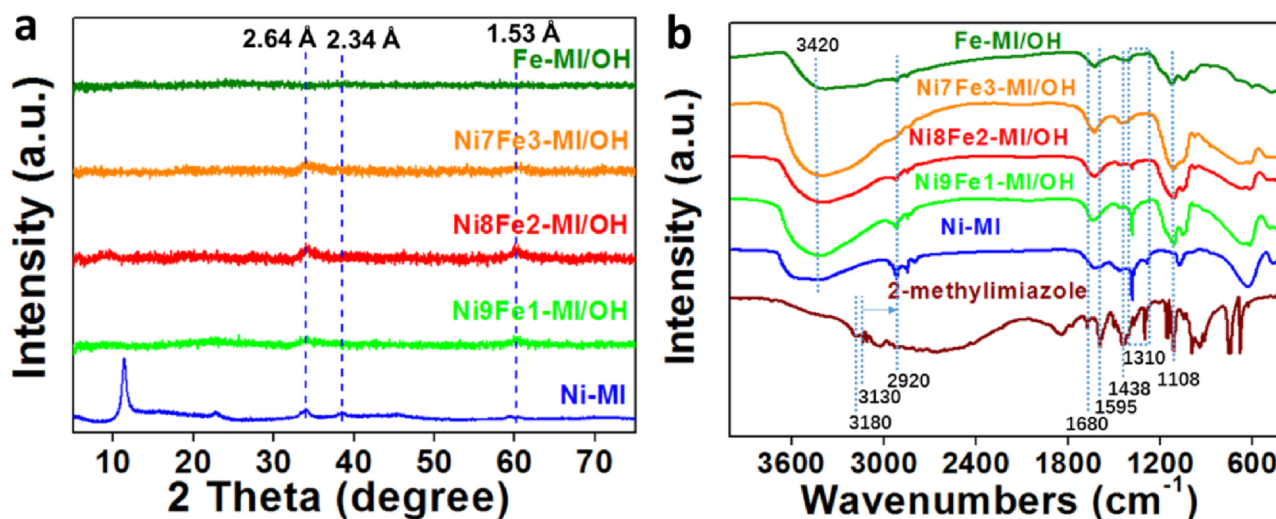**Scheme 1.** Schematic diagram of the fabrication of Ni/Fe-MI/OH.

Fig. 1. (a) XRD patterns of the Ni-MI, Ni9Fe1-MI/OH, Ni8Fe2-MI/OH, Ni7Fe3-MI/OH, and Fe-MI/OH. (b) FT-IR spectra of Ni-MI, Ni9Fe1-MI/OH, Ni8Fe2-MI/OH, Ni7Fe3-MI/OH, Fe-MI/OH, and 2-MI.

(Fig. 2a) [29]. For Fe $2p_{3/2}$ spectrum (Fig. 2b), the peaks at 712.5 and 706.2 eV belong to the Fe^{2+} and low binding energy "pre-peak", respectively [30,31]. In the N 1s spectrum (Fig. 2c), two surface components are noticed. The peaks at 398.6 and 399.6 eV correspond to the N in C-N = C aromatic rings of 2-MI and N-Ni/Fe bonds, respectively [32–35]. The C 1s XPS spectrum (Fig. S5b) can be fitted to three main peaks attributed to C–C (284.6 eV), C=N (285.0 eV), and C-N (285.9 eV) [33,36]. The XPS results of N and C can further affirm the existence of 2-MI in the final product. What's more, the O 1s XPS spectrum can be deconvoluted into three peaks (Fig. 2d), corresponding to Ni(Fe)-O (531.0 eV), –OH (531.8 eV), and absorbed water (532.6 eV) [17,29]. The XPS spectra of N 1s and O 1s further clarified that the coordination atoms between Ni/Fe species and the hybrid ligands are N and O atoms. The other Ni/Fe-MI/OH catalysts show a relative intensity similar to Ni8Fe2-MI/OH, indicating that the coordination and element environment of all samples are the same (Fig. S5a). The XPS results indicate that the same coordination of metal and 2-MI/OH ligands are present in all samples except Ni-MI, which contributes to the low-crystalline characteristic.

The structure and composition of Ni8Fe2-MI (powder) were further analyzed by TEM. The Ni8Fe2-MI powder is composed of micro-spherical particles constructed by tiny nanosheets (Fig. 3b), exhibiting the same sheet-like morphology with the Ni8Fe2-MI grown on NF (Fig. 3a). High-resolution TEM (HRTEM, Fig. 3c) shows small crystal-line regions and amorphous boundaries co-exist in the nanosheets. The measured lattice fringes of 1.53, 2.34, and 2.64 Å in the crystalline regions are consistent with that calculated from the XRD via Bragg's law. The SAED (inset in Fig. 3c) pattern displays three weak and continuous diffraction rings correspondingly. Besides, the spacing calculated from each ring agrees well with that observed in the HRTEM image, illustrating that Ni8Fe2-MI consists of numerous tiny domains with low crystallinity. From the above characterizations, one can tell that the Ni8Fe2-MI has a long-range disordered and short-range ordered structure, which is characteristic of MCCs. HAADF-STEM and EDX tests were also carried out to gain more structural and compositional information. As shown in Fig. 3d-i, elements of Ni, Fe, C, N, and O are very uniformly distributed, among which, N and O may respectively come from 2-MI and –OH, demonstrating that Ni/Fe based bimetallic coordination complexes with hybrid ligands of 2-MI and –OH are successfully obtained. In Fig. S6, the EDX elemental spectrum of Ni8Fe2-MI/OH is also provided, where the chemical formula could be regarded as $Ni_{17.3}Fe_{4.8}-(MI)_{1.5}/(OH)_{42.7}$ (See Fig. S6 for more calculation details). According to the elemental analysis of EDX, the inferred chemical formula of Ni8Fe2-MI/OH is $Ni_{17.3}Fe_{4.8}-(MI)_{1.5}/(OH)_{42.7}$,
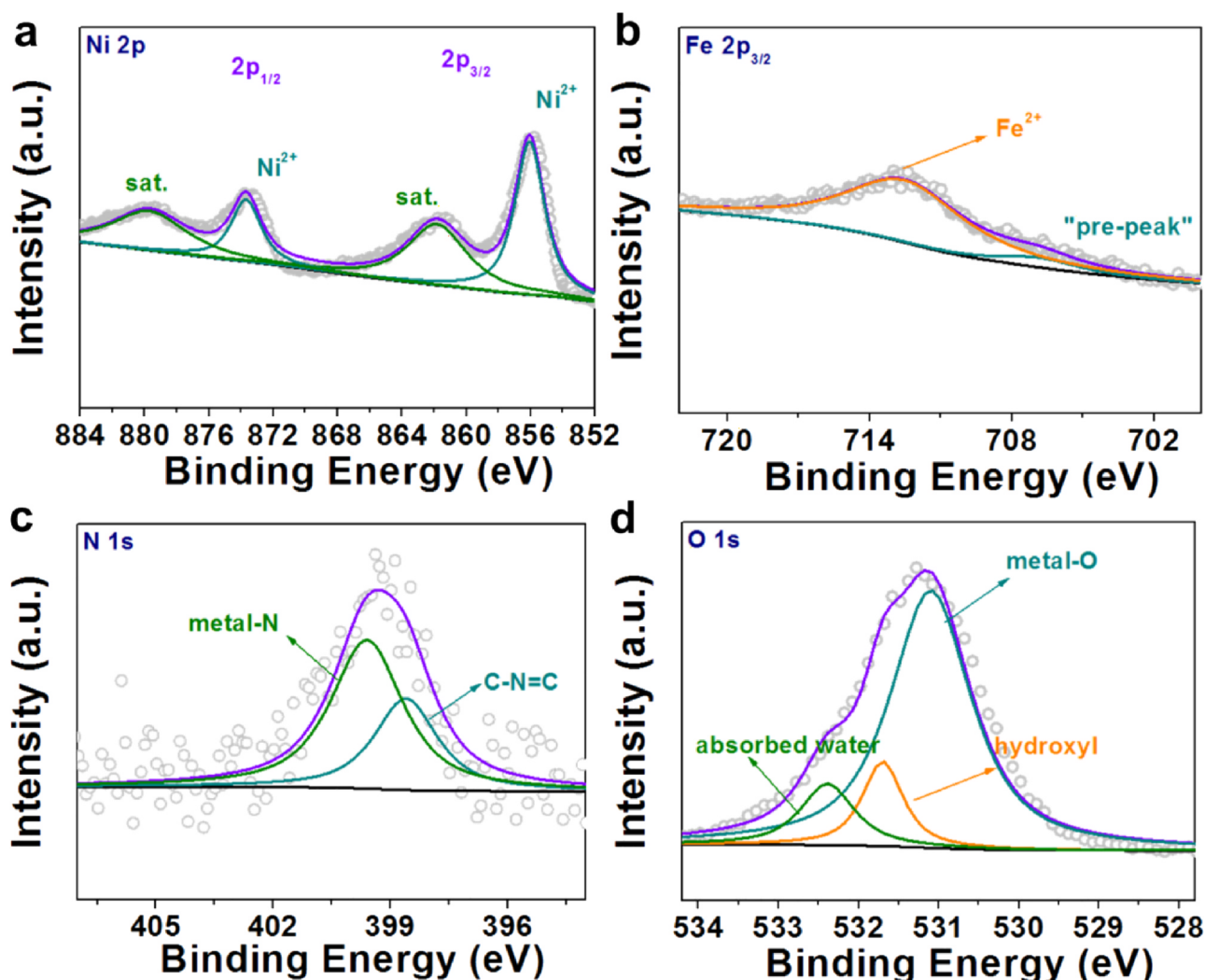
Fig. 2. XPS spectra of the Ni8Fe2-MI/OH: (a) Ni 2p, (b) Fe 2p, (c) N 1s, and (d) O 1s spectra.

which is close to the actual composition.

Electrocatalytic OER performances of NiFe-MI/OH and commercial IrO$_2$ loaded on NF were tested with a three-electrode system. The as-prepared samples grown or loaded on NF (cut into 1.0 cm^2 pieces) were directly employed as the WE. LSV curves were collected at a scan rate of 5 mV s^{-1}. "Unsmooth" LSV curves are observed (Fig. 4a) due to the generation and accumulation of oxygen bubbles under high current density, and this phenomenon has also been observed in previous reports [16,37]. For the Ni-containing samples, there is an obvious Ni^{2+}/Ni^{3+} oxidation peak at around 1.37 V [38], which might overlap with actual onset potential. Despite the existence of Ni^{2+}/Ni^{3+} oxidation peak, the onset potential of the samples can be generally determined. The Ni8Fe2-MI/OH exhibits a lower onset potential (~1.45 V) when compared to Ni-MI (~1.5 V), Ni9Fe1-MI/OH (~1.46 V), Ni7Fe3-MI/OH (~1.47 V), Fe-MI/OH (~1.49 V), and IrO$_2$ (~1.49 V) (Fig. 4a). At a current density of 10 mA cm^{-2}, the overpotential of Ni8Fe2-MI/OH is only 229 mV. The overpotential of Ni8Fe2-MI/OH is the smallest among those of Ni-MI (286 mV), Ni9Fe1-MI/OH (250 mV), Ni7Fe3-MI/OH (260 mV), Fe-MI/OH (310 mV), and IrO$_2$ (305 mV). Tafel plots are displayed in Fig. 4b to analyze the reaction kinetics during the OER process. The measured Tafel slopes are 143, 72, 30, 45, 59, and 77 mV dec^{-1} for Ni-MI, Ni9Fe1-MI/OH, Ni8Fe2-MI/OH, Ni7Fe3-MI/OH, Fe-MI/OH, and IrO$_2$, respectively. The Ni8Fe2-MI/OH presents the lowest Tafel slope, indicating its superior reaction kinetics among all the catalysts. Moreover, as summarized in Fig. 4c and Table S1, Ni8Fe2-MI/

OH also exhibits significant advantages over the reported OER catalysts.

To figure out the reasons for the outstanding OER performance of Ni8Fe2-MI/OH, ECSAs and electrochemical impedance spectroscopy (EIS) data of all the samples are provided. ECSAs were calculated from the C$_{dl}$ by measuring the CV profiles in the non-Faradaic potential region (Fig. S7). Specially, the C$_{dl}$ values for Ni-MI, Ni9Fe1-MI/OH, Ni8Fe2-MI/OH, Ni7Fe3-MI/OH, Fe-MI/OH, and IrO$_2$ are determined to be 3.34, 1.63, 2.12, 1.83, 1.49, and 22.1 mF cm^{-2}, respectively (Fig. 4d and Fig. S8a). It should be pointed out that the C$_{dl}$ of IrO$_2$ is higher than that of Ni8Fe2-MI/OH, which is contrary to the trend of LSV curves observed in Fig. 4a. Since C$_{dl}$ reflects the exposed ECSA of catalysts, while the LSV curve is commonly used to characterize the current responses at different potentials, thus, there is not necessarily a positive correlation between them and similar phenomenon can also be observed in previous works [17,39]. For the as-prepared catalysts, Ni8Fe2-MI/OH has a relatively high C$_{dl}$ value, which ranks the highest level among all bimetallic catalysts. Larger ECSA can increase electrode–electrolyte contact, and more active sites can thus be efficiently exposed to reaction species, which is one of the reasons why Ni8Fe2-MI/OH has the best performance among the bimetallic catalysts. To exclude the contribution from NF, the electrocatalytic performances of Ni/Fe-MI/OH powders are also measured, and the performance trend is consistent with that of Ni/Fe-MI/OH grown on NF (Fig. S8b-c). TOF of NiFe-MI/OH powders are also calculated at the overpotential of 330 mV. As depicted in Fig. S9, the TOF of Ni8Fe2-MI/OH is 0.125 s^{-1},
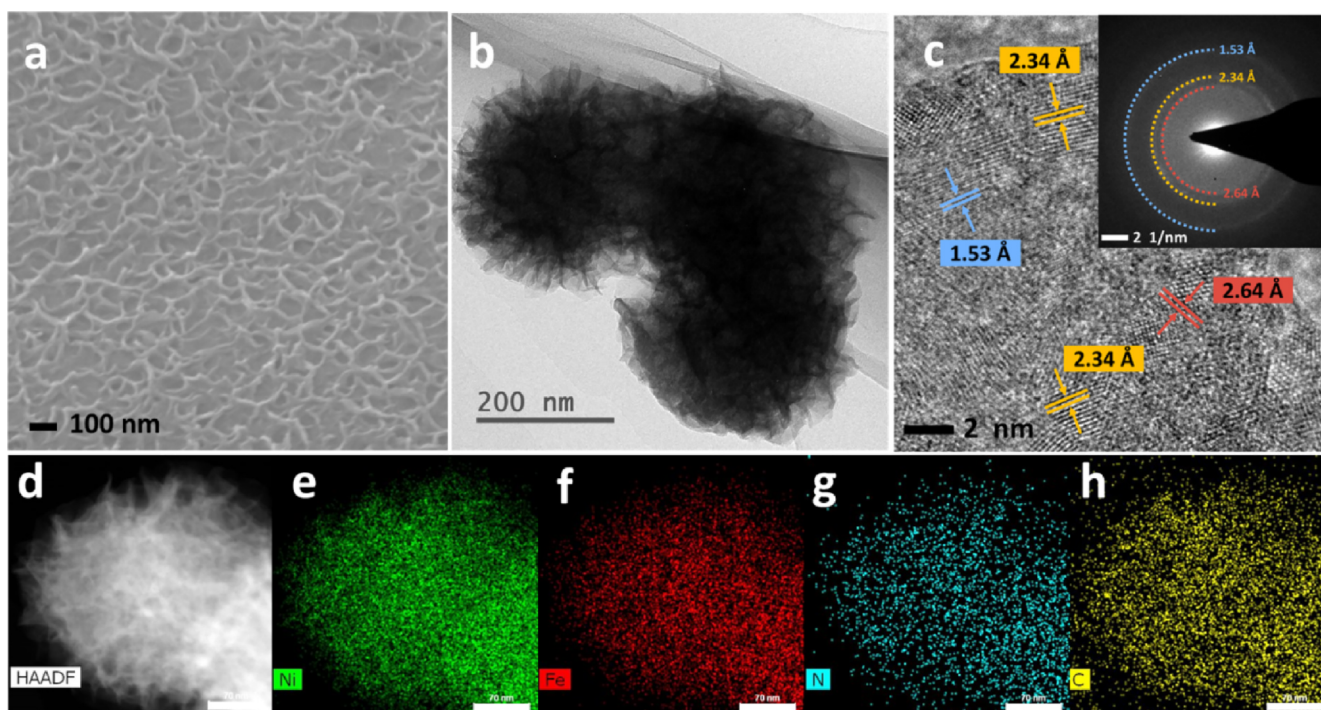
Fig. 3. (a) SEM image of Ni8Fe2-MI/OH grown on NF. (b) TEM of Ni8Fe2-MI/OH (powder) and corresponding c) HRTEM images; the inset in (c) is the corresponding SAED pattern. (d) HAADF-STEM image of Ni8Fe2-MI/OH and EDX mappings of (e) Ni, (f) Fe, (g) N, (h) C, and (i) O (scale bars for d-i: 70 nm).

which is much larger than those of Ni9Fe1-MI/OH (0.046 s^{-1}) and Ni7Fe3-MI/OH (0.035 s^{-1}). The reaction rate is almost three- to four-fold higher than those of Ni9Fe1-MI/OH and Ni7Fe3-MI/OH, illustrating that the reaction kinetics on average single active site of Ni8Fe2-MI/OH is the fastest. Since the ECSA is an important parameter that reflects the surface area exposed in the electrochemical process of OER, the ECSA-normalized current density is more reliable to evaluate the intrinsic OER activity of catalysts. Thus, LSV and Tafel plots normalized by ECSA are also presented (Fig. S10). After normalization, the Ni8Fe2-MI/OH still affords the lowest overpotential (230 mV at 10 mA cm^{-2}) and the smallest Tafel slope of 26 mV dec^{-1}. The above results indicate that Ni8Fe2-MI/OH shows the best OER intrinsic activity, consistent with the above drawn conclusion.

EIS tests were further carried out to illustrate the charge transfer capability. As presented in Fig. 4e, Ni8Fe2-MI/OH exhibits an obviously lower charge transfer resistance (R_{ct}) of ~0.34 ohm when compared to Ni-MI (~2.4 ohm), Ni9Fe1-MI/OH (~1.1 ohm), Ni7Fe3-MI/OH (~0.86 ohm), Fe-MI/OH (~1.5 ohm), and IrO$_2$ (~0.7 ohm), demonstrating that the Ni8Fe2-MI/OH can ensure the fastest charge transfer during OER process. The same EIS trend can also be noticed in the powder-based results (Fig. S8d). The semicircle-like Nyquist plots in Fig. 4e and S8d indicate that the OER process is dominated by charge transfer[40,41], which is consistent with previous reports [38,39].

In addition to higher ECSA and faster charge transfer, the bimetallic synergy of Ni/Fe is another important reason for the outstanding OER performance of Ni8Fe2-MI/OH. Compared with Ni-MI and Fe-MI/OH, a slight binding energy increase of Ni and a slight binding energy decrease of Fe can be observed in Ni8Fe2-MI/OH, respectively (Fig. S11), suggesting there is an electronic pull from Ni to Fe. As previously reported [42], the partial electron loss at Ni sites would result in higher electron affinity, thus facilitating OH$^-$ adsorption and charge transfer from the adsorbed OH$^-$ for OER. As Ni sites are the majority among active sites in Ni8Fe2-MI/OH, the catalytic performance of OER can thus be significantly enhanced when Ni sites are strengthened due to the above synergistic effect between Ni and Fe.

What's more, the Ni8Fe2-MI/OH presents robust stability. Almost no polarization increase can be observed during the long-term stability

test in 1 M KOH at the current densities of 10 and 100 mA cm^{-2} for 20 h (Fig. 4f). To get insight into the coordination environment evolution of metal ions and surrounding ligands during OER, *ex-situ* XPS of Ni8Fe2-MI/OH after 2 h stability test was carried out (Fig. S12). The characteristic peaks of Ni, Fe, N, C, and O can also be detected as the pristine sample, and almost no changes in relative intensity can be observed after the OER process. The slight decrease of N 1s spectrum (Fig. S12d) and C-N bonds in C 1s spectrum (Fig. S12e) is probably caused by the slight change in surface during the OER process. Furthermore, the *ex-situ* TEM of Ni8Fe2-MI/OH after 2 h stability test was also carried out (Fig. S13). After a 2 h stability test, the Ni8Fe2-MI/OH does not show obvious difference when compared with the pristine sample (Fig. S13a). Particularly, in HRTEM, it is clear that the nanosheets are still composed of nanocrystals and amorphous areas due to the long-range disordered structure (Fig. S13b). Thus, we can confirm the nanosheet-like structure is very stable during OER process, which is also proved in Fig. 4d. Besides, the lattice fringes are 1.5 Å, 2.2 Å, and 2.6 Å, agreeing with SAED result (Fig. S13c). HAADF-STEM images and the EDX elements mapping further reveal the uniform distribution of Ni, Fe, N, C, and O is well kept after OER (Fig. S13 d-i). All the results demonstrate the Ni8Fe2-MI/OH possesses excellent stability in the OER process.

To be summarized, the remarkable OER performance of Ni8Fe2-MI/OH can be attributed to the following factors. First, the rich amorphous boundaries between MCC nanocrystals provide abundant active sites. Second, the optimized metal ratio can bring bimetallic synergistic effect and fast charge transfer can be achieved. Third, the nanosheet-like structure can guarantee fast kinetics of the chemical reaction and fast mass transport.

4. Conclusion

In summary, Ni/Fe based bimetallic metal coordination complexes (MCCs) with rich active sites residing in the nanocrystal boundaries are designed. The coordination mechanism between bimetallic ions and hybrid ligands is verified: the crystalline structure of Ni-MI (Ni-ZIF) is broken with the introduction of Fe^{2+} ions, and MCCs are thus formed
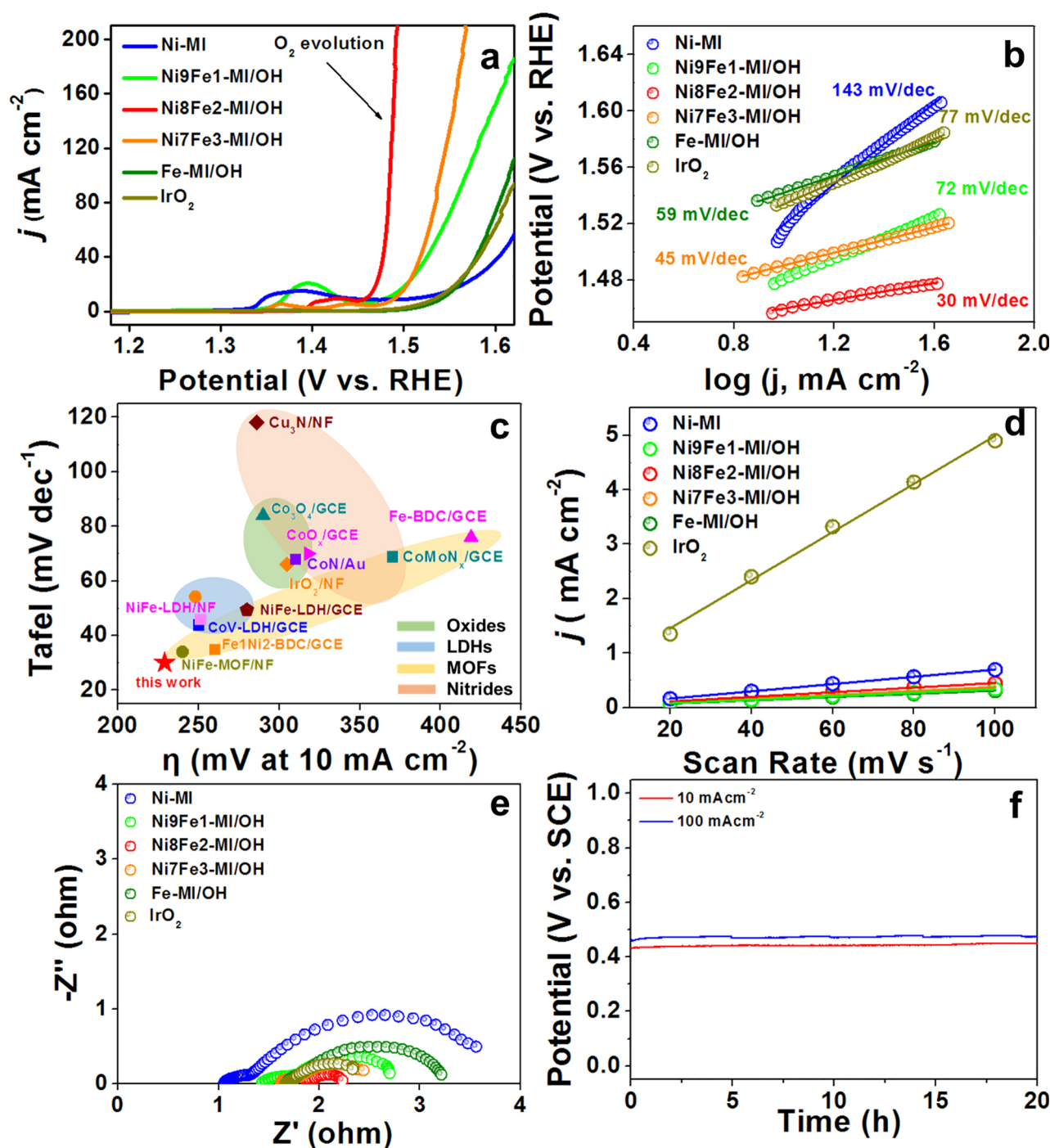
Fig. 4. Electrochemical performance of Ni-MI, Ni9Fe1-MI/OH, Ni8Fe2-MI/OH, Ni7Fe3-MI/OH, Fe-MI/OH, and IrO₂: (a) LSV curves in 1 M KOH at a scan rate of 5 mV s⁻¹ and (b) corresponding Tafel plots. (c) Comparison of Tafel slope and overpotential for Ni8Fe2-MI/OH and previously reported OER catalysts in alkaline electrolytes. Detailed data in (c) were obtained from references as shown in Table S1, and different circle color represents a different type of common catalysts such as oxides, LDHs, MOFs, and nitrides. (d) CV current density versus scan rate and the linear slope is equal to that of C_{dl}. (e) EIS Nyquist plots. (f) Durability test of Ni8Fe2-MI/OH in 1 M KOH at constant current densities of 10 and 100 mAcm⁻² (with iR correction).

via the coordination between bimetallic ions (Ni^{2+} and Fe^{2+}) and hybrid ligands (2-MI and –OH). The rich active sites derived from the long-range disordered but short-range ordered structure of MCCs, the bimetallic synergistic effect as well as the quick mass transfer capability of nanosheet-like structure, could together promote the electrocatalytic performance for OER. Specially, the achieved Ni8Fe2-MI/OH exhibits excellent OER performance in alkaline solution: overpotential is as low as 229 mV at a current density of 10 mA cm⁻², which is superior to noble metal catalyst IrO₂ and most of the reported catalysts. Our findings open up a new avenue to coordination mechanism of MCCs, and emphasize the critical role of transitional bimetallic coordination complexes for OER catalysts.

Declaration of Competing Interest

The authors declare that they have no known competing financial interests or personal relationships that could have appeared to influence the work reported in this paper.

Acknowledgements

Appendix A. Supplementary data

Supplementary data to this article can be found online at https://doi.org/10.1016/j.cej.2020.126959.

References

[1] L. Li, P. Wang, Q. Shao, X. Huang, Metallic nanostructures with low dimensionality for electrochemical water splitting, Chem. Soc. Rev. 49 (2020) 3072–3106, https://doi.org/10.1039/D0CS00013B.

[2] Y. Hou, Z. Wen, S. Cui, S. Ci, S. Mao, J. Chen, Hybrid electrocatalysis: an advanced nitrogen-doped graphene/cobalt-embedded porous carbon polyhedron hybrid for efficient catalysis of oxygen reduction and water splitting, Adv. Funct. Mater. 25 (2015) 872–882, https://doi.org/10.1002/adfm.201570041.

[3] S. Tan, Y. Pan, Q. Wei, Y. Jiang, F. Xiong, X. Yao, Z. Cai, Q. An, L. Zhou, L. Mai, Polyol solvation effect on tuning the universal growth of binary metal oxide nanodots@ graphene oxide heterostructures for electrochemical applications, Chem.-Eur. J. 25 (2019) 14604–14612, https://doi.org/10.1002/chem.201902697.

[4] Z. Wen, S. Ci, Y. Hou, J. Chen, Facile one-pot, one-step synthesis of a carbon nanoarchitecture for an advanced multifunctonal electrocatalyst, Angew. Chem. Int. Ed. 53 (2014) 6496–6500, https://doi.org/10.1002/anie.201402574.

[5] N.-T. Suen, S.-F. Hung, Q. Quan, N. Zhang, Y.-J. Xu, H.M. Chen, Electrocatalysis for the oxygen evolution reaction: recent development and future perspectives, Chem. Soc. Rev. 46 (2017) 337–365, https://doi.org/10.1039/C6CS00328A.

[6] X. Zhou, S. Liu, A. Xu, K. Wei, W. Han, J. Li, X. Sun, J. Shen, X. Liu, L. Wang, A multi-walled carbon nanotube electrode based on porous graphite-RuO_2 in electrochemical filter for pyrrole degradation, Chem. Eng. J. 330 (2017) 956–964, https://doi.org/10.1016/j.cej.2017.08.042.

[7] A.M. Fadl, M.I. Abdou, D. Laila, S.A. Sadeek, Fabrication and characterization of novel p-Phenylamine-N(4-chloro salicylaldenemine) ligand and its metal complexes and evaluation their anti-corrosion and chemical resistance properties in epoxy/SiO_2 nanocomposite for steel surface coating, Chem. Eng. J. 384 (2020) 123390, , https://doi.org/10.1016/j.cej.2019.123390.

[8] N.Y. Chen, B.C. Pan, A preliminary exploration on Au nanoparticles-mediated colorimetric analysis of Cr(III)-carboxyl complexes in synthetic and authentic water samples, Chem. Eng. J. 387 (2020) 124079, , https://doi.org/10.1016/j.cej.2020.124079.

[9] M.A. Rahim, M. Bjornmalm, T. Suma, M. Faria, Y. Ju, K. Kempe, M. Muellner, H. Ejima, A.D. Stickland, F. Caruso, Metal-phenolic supramolecular gelation, Angew. Chem. Int. Ed. 55 (2016) 13803–13807, https://doi.org/10.1002/anie.201608413.

[10] H. Ejima, J.J. Richardson, K. Liang, J.P. Best, M.P. van Koeverden, G.K. Such, J. Cui, F. Caruso, One-step assembly of coordination complexes for versatile film and particle engineering, Science 341 (2013) 154–157, https://doi.org/10.1126/science.1237265.

[11] J. Guo, Y. Ping, H. Ejima, K. Alt, M. Meissner, J.J. Richardson, Y. Yan, K. Peter, D. von Elverfeldt, C.E. Hagemeyer, F. Caruso, Engineering multifunctional capsules through the assembly of metal-phenolic networks, Angew. Chem. Int. Ed. 53 (2014) 5546–5551, https://doi.org/10.1002/anie.201311136.

[12] M.A. Rahim, K. Kempe, M. Muellner, H. Ejima, Y. Ju, M.P. van Koeverden, T. Suma, J.A. Braunger, M.G. Leeming, B.F. Abrahams, F. Caruso, Surface-confined amorphous films from metal-coordinated simple phenolic ligands, Chem. Mater. 27 (2015) 5825–5832, https://doi.org/10.1021/acs.chemmater.5b02790.

[13] C. Yang, G. Nikiforidis, J.Y. Park, J. Choi, Y. Luo, L. Zhang, S.-C. Wang, Y.-T. Chan, J. Lim, Z. Hou, M.-H. Baik, Y. Lee, H.R. Byon, Designing redox-stable cobalt-polypyridyl complexes for redox flow batteries: spin-crossover delocalizes excess charge, Adv. Energy Mater. 8 (2018) 1702897, https://doi.org/10.1002/aenm.201702897.

[14] C. Liu, J. Wang, J. Wan, Y. Cheng, R. Huang, C. Zhang, W. Hu, G. Wei, C. Yu, Amorphous metal-organic framework-dominated nanocomposites with both compositional and structural heterogeneity for oxygen evolution, Angew. Chem. Int. Ed. 59 (2019) 3630–3637, https://doi.org/10.1002/anie.201914587.

[15] N.L.W. Septiani, Y.V. Kaneti, K.B. Fathoni, K. Kani, A.E. Allah, B. Yuliarto, H.K. Nugraha, Z.A. Dipojono, D. Alothman, Y.Y. Golberg, Self-assembly of two-dimensional bimetallic nickel-cobalt phosphate nanoplates into one-dimensional porous chainlike architecture for efficient oxygen evolution reaction, Chem. Mater. 32 (2020) 7005–7018, https://doi.org/10.1021/acs.chemmater.0c02385.

[16] B. Suryanto, Y. Wang, R. Hocking, W. Adamson, C. Zhao, Overall electrochemical splitting of water at the heterogeneous interface of nickel and iron oxide, Nat. Commun. 10 (2019) 5599, https://doi.org/10.1038/s41467-019-13415-8.

[17] J. Li, W. Huang, M. Wang, S. Xi, J. Meng, K. Zhao, J. Jin, W. Xu, Z. Wang, X. Liu, Low-crystalline bimetallic metal–organic framework electrocatalysts with rich active sites for oxygen evolution, ACS Energy Lett. 4 (2018) 285–292, https://doi.org/10.1021/acsenergylett.8b02345.

[18] F. Dionigi, Z. Zeng, I. Sinev, T. Merzdorf, S. Deshpande, M.B. Lopez, S. Kunze, I. Zegkinoglou, H. Sarodnik, D. Fan, A. Bergmann, J. Drnec, J.F.D. Araujo, M. Gliech, D. Teschner, J. Zhu, W.-X. Li, J. Greeley, B.R. Cuenya, P. Strasser, In-situ structure and catalytic mechanism of NiFe and CoFe layered double hydroxides during oxygen evolution, Nat. Commun. 11 (2020) 2522, https://doi.org/10.1038/s41467-020-16237-1.

[19] J. Meng, C. Niu, L. Xu, J. Li, X. Liu, X. Wang, Y. Wu, X. Xu, W. Chen, Q. Li, Z. Zhu, D. Zhao, L. Mai, General oriented formation of carbon nanotubes from metal-organic frameworks, J. Am. Chem. Soc. 139 (2017) 8212–8221, https://doi.org/10.1021/jacs.7b01942.

[20] T.D. Bennett, A.K. Cheetham, Amorphous metal-organic frameworks, Acc. Chem. Res. 47 (2014) 1555–1562, https://doi.org/10.1021/ar5000314.

[21] Y.I. Avilavega, C. Leyvaporras, M. Mireles, M.A. Quevedolopez, J. Macossay, J. Bonillacruz, Nitroxide-functionalized graphene oxide from graphite oxide, Carbon 63 (2013) 376–389, https://doi.org/10.1016/j.carbon.2013.06.093.

[22] K.-Y.A. Lin, H.-A. Chang, Ultra-high adsorption capacity of zeolitic imidazole framework-67 (ZIF-67) for removal of malachite green from water, Chemosphere 139 (2015) 624–631, https://doi.org/10.1016/j.chemosphere.2015.01.041.

[23] H. Xia, J. Zhang, Z. Yang, S. Guo, S. Guo, Q. Xu, 2D MOF nanoflake-assembled spherical microstructures for enhanced supercapacitor and electrocatalysis performances, Nano-Micro Lett. 9 (2017) 43, https://doi.org/10.1007/s40820-017-0144-6.

[24] W. Chen, J. Fang, Y. Zhang, G. Chen, S. Zhao, R. Huang, Y. Zhou, Morphological and structure dual modulation of cobalt-based layer double hydroxides by Ni doping and 2-methylimidazole inducting as bifunctional electrocatalysts for overall water splitting, J. Power Sources 400 (2018) 172–182, https://doi.org/10.1016/j.jpowsour.2018.08.023.

[25] D.A. Carter, J.E. Pemberton, Raman spectroscopy and vibrational assignments of 1- and 2-methylimidazole, J. Raman Spectrosc. 28 (1997) 939–946, https://doi.org/10.1002/(SICI)1097-4555(199712)28:123.0.CO;2-R.

[26] C. Kuai, Y. Zhang, D. Wu, D. Sokaras, L. Mu, S. Spence, D. Nordlund, F. Lin, X.-W. Du, Fully oxidized Ni–Fe layered double hydroxide with 100% exposed active sites for catalyzing oxygen evolution reaction, ACS Catal. 9 (2019) 6027–6032, https://doi.org/10.1021/acscatal.9b01935.

[27] T. Wang, S. Zhang, X. Yan, M. Lyu, L. Wang, J. Bell, H. Wang, 2-methylimidazole-derived Ni-Co layered double hydroxide nanosheets as high rate capability and high energy density storage material in hybrid supercapacitors, ACS Appl. Mater. Interfaces 9 (2017) 15510–15524, https://doi.org/10.1021/acsami.7b02987.

[28] P. Vialat, C. Mousty, C. Taviot-Gueho, G. Renaudin, H. Martinez, J.-C. Dupin, E. Elkaim, F. Leroux, High-performing monometallic cobalt layered double hydroxide supercapacitor with defined local structure, Adv. Funct. Mater. 24 (2014) 4831–4842, https://doi.org/10.1002/adfm.201400310.

[29] Z. Dong, F. Lin, Y. Yao, L. Jiao, Crystalline $Ni(OH)_2$/amorphous NiMoOx mixed-catalyst with Pt-like performance for hydrogen production, Adv. Energy Mater. 9 (2019) 1902703, https://doi.org/10.1002/aenm.201902703.

[30] J. Xing, K. Guo, Z. Zou, M. Cai, J. Du, C. Xu, In situ growth of well-ordered NiFe-MOF-74 on Ni foam by Fe^{2+} induction as an efficient and stable electrocatalyst for water oxidation, Chem. Commun. 54 (2018) 7046–7049, https://doi.org/10.1039/C8CC03112F.

[31] A.P. Grosvenor, B.A. Kobe, M.C. Biesinger, N.S. McIntyre, Investigation of multiplet splitting of Fe 2p XPS spectra and bonding in iron compounds, Surf. Interface Anal. 36 (2004) 1564–1574, https://doi.org/10.1002/sia.1984.

[32] J. Yang, F. Zhang, H. Lu, X. Hong, H. Jiang, Y. Wu, Y. Li, Hollow Zn/Co ZIF particles derived from core-shell ZIF-67@ZIF-8 as selective catalyst for the semi-hydrogenation of acetylene, Angew. Chem. Int. Ed. 54 (2015) 10889–10893, https://doi.org/10.1002/anie.201504242.

[33] Y. Wu, X. Song, S. Xu, J. Zhang, Y. Zhu, L. Gao, G. Xiao, 2-methylimidazole modified Co-BTC MOF as an efficient catalyst for chemical fixation of carbon dioxide, Catal. Lett. 149 (2019) 2575–2585, https://doi.org/10.1007/s10562-019-02874-9.

[34] J. Yang, X. Wang, B. Li, L. Ma, L. Shi, Y. Xiong, H. Xu, Novel iron/cobalt-containing polypyrrole hydrogel-derived trifunctional electrocatalyst for self-powered overall water splitting, Adv. Funct. Mater. 27 (2017) 1606497, https://doi.org/10.1002/adfm.201606497.

[35] D. Koshy, S. Chen, D. Lee, M. Stevens, A. Abdellah, S. Dull, G. Chen, D. Nordlund, A. Gallo, C. Hahn, D. Higgins, Z. Bao, T. Jaramillo, Understanding the origin of highly selective CO_2 electroreduction to CO on Ni, N-doped carbon catalysts, Angew. Chem. Int. Ed. 132 (2020) 4072–4079, https://doi.org/10.1002/ange.201912857.

[36] J. Yang, G. Zhu, Y. Liu, J. Xia, Z. Ji, X. Shen, S. Wu, Fe_3O_4-decorated Co_9S_8 nanoparticles in situ grown on reduced graphene oxide: a new and efficient electrocatalyst for oxygen evolution reaction, Adv. Funct. Mater. 26 (2016) 4712–4721, https://doi.org/10.1002/adfm.201600674.

[37] B. Zhang, C. Zhu, Z. Wu, E. Stavitski, Y.H. Lui, T.-H. Kim, H. Liu, L. Huang, X. Luan, L. Zhou, K. Jiang, W. Huang, S. Hu, H. Wang, J.S. Francisco, Integrating Rh species with NiFe-layered double hydroxide for overall water splitting, Nano Lett. 20 (2020) 136–144, https://doi.org/10.1021/acs.nanolett.9b03460.

[38] Z. Xue, X. Li, Q. Liu, M. Cai, K. Liu, M. Liu, Z. Ke, X. Liu, G. Li, Interfacial electronic structure modulation of NiTe nanoarrays with NiS nanodots facilitates electrocatalytic oxygen evolution, Adv. Mater. 31 (2019) 1900430, https://doi.org/10.1002/adma.201900430.

[39] Y. Liu, Y. Ying, L. Fei, Y. Liu, Q. Hu, G. Zhang, S.Y. Pang, W. Lu, C.L. Mak, X. Luo, L. Zhou, M. Wei, H. Huang, Valence engineering via selective atomic substitution on

tetrahedral sites in spinel oxide for highly enhanced oxygen evolution catalysis, J. Am. Chem. Soc. 141 (2019) 8136–8145, https://doi.org/10.1021/jacs.8b13701.

[40] X.R. Nóvoa, C. Pérez, Electrochemical impedance spectroscopy, Electrochim. Acta 252 (2017), https://doi.org/10.1016/j.electacta.2017.08.138.

[41] M. Orazem, B. Tribollet, A tutorial on electrochemical impedance spectroscopy, ChemTexts 6 (2020), https://doi.org/10.1007/s40828-020-0110-7.

[42] Q. Zhao, J. Yang, M. Liu, R. Wang, G. Zhang, H. Wang, H. Tang, C. Liu, Z. Mei, H. Chen, F. Pan, Tuning electronic push/pull of Ni-based hydroxides to enhance hydrogen and oxygen evolution reactions for water splitting, ACS Catal. 8 (2018) 5621–5629, https://doi.org/10.1021/acscatal.8b01567.